Quantum tunneling rotor as a sensitive atomistic probe of guests in a metal-organic framework

Kirill Titov,[1] Matthew R. Ryder ⬚,[1,2,3] Aran Lamaire ⬚,[4] Zhixin Zeng,[1] Abhijeet K. Chaudhari,[1,5] James Taylor,[2]
E. M. Mahdi ⬚,[1] Sven M. J. Rogge ⬚,[4] Sanghamitra Mukhopadhyay ⬚,[2] Svemir Rudić ⬚,[2,*] Veronique Van Speybroeck ⬚,[4,†]
Felix Fernandez-Alonso ⬚,[6,7,8,9,‡] and Jin-Chong Tan ⬚[1,§]

[1]*Multifunctional Materials & Composites (MMC) Laboratory, Department of Engineering Science,*
University of Oxford, Parks Road, Oxford OX1 3PJ, United Kingdom
[2]*ISIS Neutron and Muon Source, Science and Technology Facility Council, UKRI,*
Rutherford Appleton Laboratory, Chilton, Didcot OX11 0QX, United Kingdom
[3]*Materials Science and Technology Division, Oak Ridge National Laboratory, Oak Ridge, Tennessee 37831, USA*
[4]*Center for Molecular Modeling (CMM), Ghent University, Technologiepark-Zwijnaarde 46, 9052 Zwijnaarde, Belgium*
[5]*Department of Chemistry, Christ University, Hosur Road, Bangalore 560029, India*
[6]*Materials Physics Center, CSIC-UPV/EHU, Paseo Manuel de Lardizabal 5, 20018 Donostia - San Sebastian, Spain*
[7]*Donostia International Physics Center (DIPC), Paseo Manuel de Lardizabal 4, 20018 Donostia - San Sebastian, Spain*
[8]*Department of Physics and Astronomy, University College London, Gower Street, London WC1E 6BT, United Kingdom*
[9]*IKERBASQUE, Basque Foundation for Science, Plaza Euskadi 5, 48009 Bilbao, Spain*

Quantum tunneling rotors in a zeolitic imidazolate framework ZIF-8 can provide insights into local gas adsorption sites and local dynamics of porous structure, which are inaccessible to standard physisorption or x-ray diffraction sensitive primarily to long-range order. Using *in situ* high-resolution inelastic neutron scattering at 3 K, we follow the evolution of methyl tunneling with respect to the number of dosed gas molecules. While nitrogen adsorption decreases the energy of the tunneling peak, and ultimately hinders it completely (0.33 meV to zero), argon substantially increases the energy to 0.42 meV. *Ab initio* calculations of the rotational barrier of ZIF-8 show an exception to the reported adsorption sites hierarchy, resulting in anomalous adsorption behavior and linker dynamics at subatmospheric pressure. The findings reveal quantum tunneling rotors in metal-organic frameworks as a sensitive atomistic probe of local physicochemical phenomena.

I. INTRODUCTION

Gas adsorption studies are ubiquitous in metal-organic framework (MOF) research. Nevertheless, conflicting reports of MOF behavior persist in the literature, for example, on the fundamental question of structural flexibility [1] vs rigidity [2] because the information provided by gas adsorption experiments, together with other long-range techniques such as x-ray diffraction (XRD), is not always sufficient to advance the understanding of dynamic and transient phenomena [3]. Likewise, research on molecular rotors in MOFs is gaining attention, revealing a range of rotational linker dynamics (either free or hindered motions) [4,5] with implications on physical and chemical properties of the framework structure

[6]. The much-contested behavior of a widely studied MOF, Zeolitic Imidazolate Framework-8 (ZIF-8), is a case in point. ZIF-8′s so-called gate-opening behavior [1], and its linker movements in general [7,8], are still not fully understood despite 25 years of active research [9]. Inelastic neutron scattering (INS) [10], specifically by quantum rotational tunneling of methyl ($-CH_3$) groups in ZIF-8, offers the possibility to resolve many unanswered questions. Rotational tunneling is the phenomenon of the librational states of a molecule whose rotating atoms, in this case, the three H atoms, are indistinguishable [11,12] and is illustrated schematically in Fig. 1(a). These methyl rotors, which account for 24 $-CH_3$ groups for each unit cell of ZIF-8, are sensitive to changes in the surrounding potentials and, therefore, can act as local probes of their atomic environments inside the framework pores. This sprawling network of quantum tunneling sensors can be harnessed to track gas adsorption processes, revealing local mechanisms at the atomic level. Although the methyl rotor in an empty ZIF-8 has been previously linked to quantum tunneling by Yildirim *et al.* [13], they have not investigated the effect of gas dosing on the tunneling phenomenon.

Early studies of the ZIF-8 structure and its behavior in response to gases recognized two extreme states, mainly defined by the orientation of the 2-methylimidazolate (mIm) linker, termed the "closed" and "open" gate. The exact mechanism
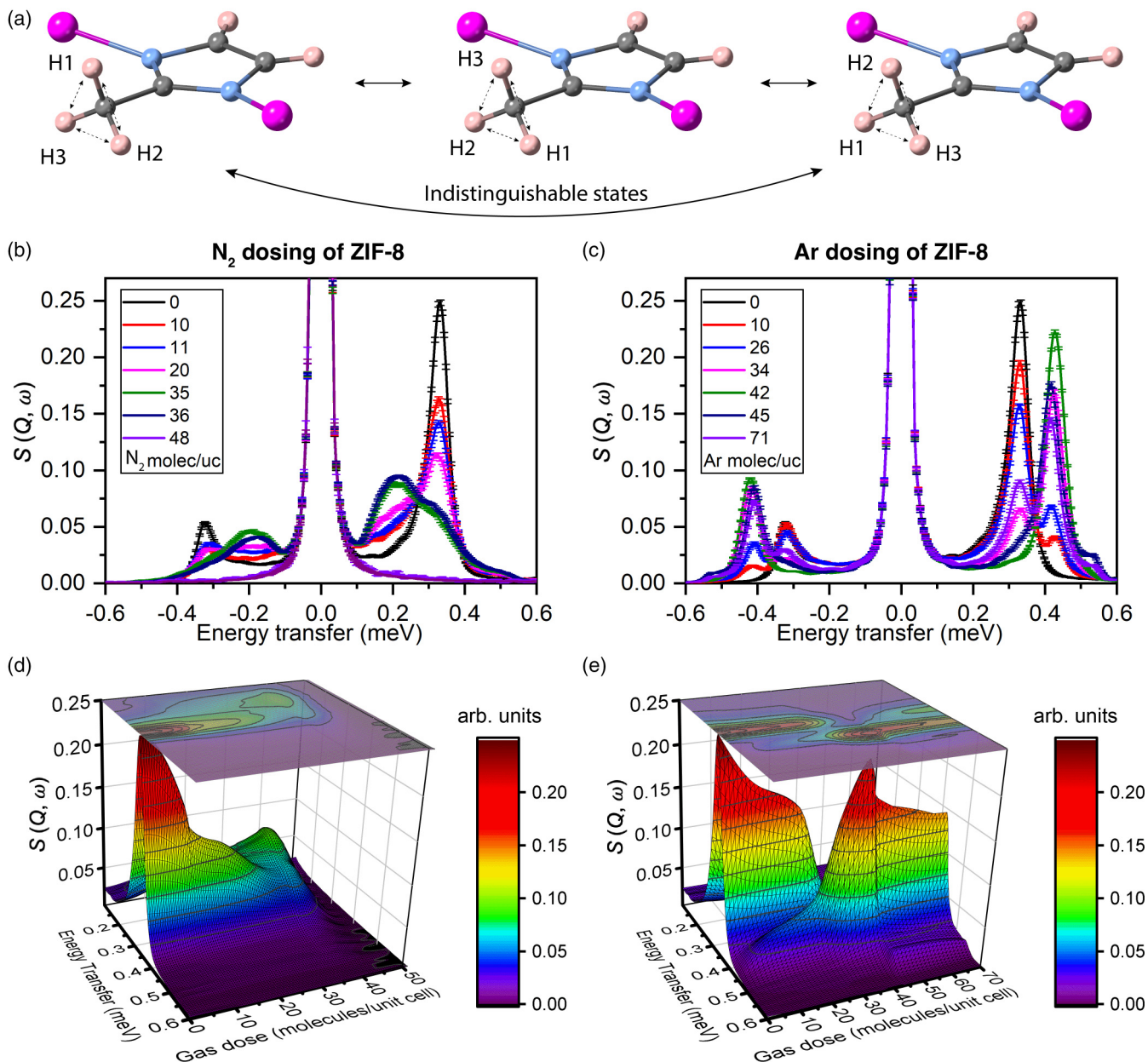
FIG. 1. Methyl tunneling in ZIF-8 with adsorbed guests, measured at 3 K. (a) Indistinguishable librational states of CH_3 rotors in ZIF-8 under quantum rotational tunneling. Color scheme: Zn (pink), C (gray), N (blue), and H (beige). (b), (c) Inelastic neutron-scattering (INS) spectra (collected at 3 K) of ZIF-8 powder dosed at 77 K with varying amounts of N_2 and Ar gas, respectively. (d), (e) Three-dimensional interpolated surfaces of INS spectra in (b) and (c), respectively.

behind the transformation was unclear and was complicated by the experimental technique—applying high hydrostatic pressure to a single crystal and tracking averaged structural changes in XRD patterns [14]. Based on these observations, it was recognized that both states were needed to simulate the gas adsorption behavior of ZIF-8 [1,15], but the existence of preferential adsorption sites was rejected based on early theoretical studies [16]. Subsequent studies, which included INS experiments and density-functional theory calculations of terahertz (THz) vibrational modes of ZIF-8, revealed that the linker orientation could change dynamically, including via "swing" motions of intermediate states that would open and close the pore window aperture into the sodalite cage without

the need for guest adsorption [7]. Further experiments showed these motions in THz spectroscopy [17,18] and nuclear magnetic resonance experiments [19], which in conjunction with theoretical simulations have identified multiple vibrational motions of the ZIF-8's structural moieties. By simulating and synthesizing ZIF-8 variants with various substitutes for the $-CH_3$ groups of mIm linkers, it was also shown that these motions were affected by the chemistry of the framework, which in turn affected gas adsorption behavior [6,20–23]. The work by Moggach and co-workers [24] enriched this expanding view of ZIF-8 by showing that there exist preferential adsorption sites within the framework's pores, despite earlier suggestions [16] to the contrary. This literature, together with

our results from the local quantum tunneling probes presented here, confer a rich view of ZIF-8's behavior, whereby dynamic vibrational modes and adsorption energies at specific sites, all guided by the underlying physics and chemistry of the porous framework, play radical roles in observed phenomena.

II. EXPERIMENTAL AND THEORETICAL METHODS

A. Materials

ZIF-8 was purchased from Sigma-Aldrich. For a typical sample, 1.2 g of ZIF-8 powder (particle size ~ 1 μm) was loaded into a perforated Al sachet and evacuated at 200 °C overnight to ensure the sample was desolvated prior to the gas dosing experiments.

B. INS and neutron powder diffraction

The high-resolution INS and neutron powder-diffraction (NPD) data [10,25,26] were collected on the OSIRIS spectrometer at the ISIS Pulsed Neutron and Muon Source at the Rutherford Appleton Laboratory in Chilton, UK. OSIRIS is a high-resolution (25.4 μeV) indirect-geometry neutron spectrometer with long-wavelength diffraction capabilities [27–29]. The secondary spectrometer is positioned at ~ 34 m from the 25 K liquid hydrogen moderator. Optimized for low-energy, high-resolution inelastic neutron-scattering studies, OSIRIS uses a broadband of incident wavelengths which are Bragg scattered from a crystal-analyzer array following interaction with the sample. For the INS experiment, the (002) plane of the pyrolytic graphite analyzer was used, thus defining the single final energy of detected neutrons as 1.84 meV. The cooled beryllium filter between the sample and the analyzer suppressed higher-order reflections of the graphite analyzer. Due to utilizing a pulsed neutron source, time-of-flight methods are used to determine energies at each particular scattering angle. Using the repetition rate of 16 Hz, which is one-third of the repetition rate of ISIS Target Station 1, an energy transfer range of 20 meV (~ 5 THz) was achieved. The scattered neutrons were detected in an angular range corresponding to the momentum transfer (Q) range $0.42-1.82 \text{ Å}^{-1}$. The scattered data from all Q values in this range were summed up to produce the INS spectrum. The neutron-diffraction data were obtained from the instrument as a by-product of the spectroscopy experiments from diffraction detectors in the backscattered geometry. Its resolution amounts to $\Delta d/d = 2.5 \times 10^{-3}$, where Δd is the full width at half maximum of diffraction peaks in d spacing.

C. Gas dosing

The sample was loaded into a cylindrical vanadium can connected to a gas-handling system. N_2 and Ar gas loading was done volumetrically at 77 K to emulate the Brunauer-Emmett-Teller (BET) test conditions (see below) and to ensure that the sample adsorbed the gas. The sample was degassed at 10^{-7} mbar between gas dosing experiments. At each gas dose, the system was allowed to equilibrate for at least 30 min. The sample was then gradually cooled down to 3 K (within ~ 1 h), where the INS measurements were performed. This methodology of dosing at 77 K and probing at 3 K has previously been adopted to investigate the gas adsorption process within MOFs utilizing INS [30].

D. Gas adsorption measurements

BET isotherms of ZIF-8 for N_2 and Ar were measured on a Quantachrome Autosorb iQ-Chemi instrument at 77 K.

E. Electronic structure calculations

To determine the rotational energy barrier of a "methyl top" (i.e., $-CH_3$ rotor) in ZIF-8, with and without adsorbed N_2 molecules or Ar atoms, each ZIF-8 structure was optimized using CP2K [31,32] in combination with the ASE (atomic simulation environment) [33]. Given that the methyl tops in ZIF-8 behave as quasifree rotors, the energy differences associated with their rotation are very small and sensitive to minor structural differences, which makes their optimization more difficult. Therefore, the crystal symmetry (space group $I\bar{4}3m$) was kept fixed during the optimization, to maintain the equivalence of the different methyl tops. As only structures with full occupation of all equivalent N_2 or Ar adsorption sites were considered, the N_2 molecules or Ar atoms were also required to adhere to the crystal symmetry. The optimizations converged when the forces on all atoms were smaller than 0.0025 eV/Å.

Subsequently, the rotational energy barrier was obtained by rotating one of the methyl tops around the axis of the C–C bond to which it was connected. After every rotational step, an intermediate optimization was performed for the hydrogen atoms of the methyl top, as these hydrogen atoms were not necessarily equivalent due to their different local environment in the structure. During this intermediate optimization, the other atoms were kept fixed.

All the calculations used the optimal unit cell for ZIF-8, which was determined by fitting an equation of state for the empty framework (guest-free). Furthermore, all the calculations were performed using the Perdew–Burke-Ernzerhof functional with the D3 dispersion scheme and Becke-Johnson damping (PBE-D3(BJ)) [34–36], combined with Goedecker-Teter-Hutter pseudopotentials [37], a plane-wave basis set with a cutoff of 800 Ry and a relative cutoff of 60 Ry, and Gaussian TZVP-MOLOPT [38] basis sets for all elements except Ar, as for this element only a DZVP-MOLOPT basis set is available.

F. Rotational energy levels

Once the rotational energy barrier of the methyl top was determined from electronic structure calculations, as outlined in the previous section, the discrete rotational energy levels can be obtained by numerically solving the Schrödinger equation for a hindered rotor, for which we use the so-called direct matrix method [39,40]. Using Numerov's method, a fourth-order approximation to the wave function can be obtained:

$$\psi_{i+1}\left(1 + \frac{(\Delta\varphi)^2}{12} f_{i+1}\right)$$

$$= 2\psi_i\left(1 - \frac{5(\Delta\varphi)^2}{12} f_i\right) - \psi_{i-1}\left(1 + \frac{(\Delta\varphi)^2}{12} f_{i-1}\right)$$

$$+ \mathcal{O}(\Delta\varphi^6), \quad (1)$$

with $\Delta\varphi = \varphi_{i+1} - \varphi_i$, $\psi_i = \psi(\varphi_i)$, and $f_i = f(\varphi_i) = -\frac{V_i - E}{B}$. For a hindered rotor, characterized by the Hamiltonian

$$\mathcal{H} = -B\frac{d^2}{d\varphi^2} + V(\varphi), \qquad (2)$$

with

$$B = \frac{1}{2I} = \frac{1}{2\sum_i m_i r_i^2}, \qquad (3)$$

the Schrödinger equation can be rewritten as

$$-B\frac{\psi_{i-1} - 2\psi_i + \psi_{i+1}}{(\Delta\varphi)^2} + \frac{V_{i-1}\psi_{i-1} + 10V_i\psi_i + V_{i+1}\psi_{i+1}}{12}$$

$$= E\frac{\psi_{i-1} + 10\psi_i + \psi_{i+1}}{12}. \qquad (4)$$

Using the matrix representations

$$\boldsymbol{\psi} = \begin{pmatrix} \psi_1 \\ \vdots \\ \psi_i \\ \vdots \\ \psi_N \end{pmatrix}, \ \mathbf{A} = \mathbf{I}_{-1} - 2\mathbf{I}_0 + \mathbf{I}_1, \ \mathbf{C} = \mathbf{I}_{-1} + 10\mathbf{I}_0 + \mathbf{I}_1,$$

$$\mathbf{V} = \begin{pmatrix} V_1 \\ \vdots \\ V_i \\ \vdots \\ V_N \end{pmatrix}, \qquad (5)$$

with $\mathbf{I}_p$ a matrix with $[\mathbf{I}_p]_{i,i+p} = 1$ ($i \in \{1, \ldots, N\}$) and zeros elsewhere, the fourth-order Numerov approximation of the Schrödinger equation can be transformed into an eigenvalue equation:

$$-\frac{12B}{(\Delta\varphi)^2}\mathbf{C}^{-1}\mathbf{A}\boldsymbol{\psi} + \mathbf{V}\boldsymbol{\psi} = E\boldsymbol{\psi}. \qquad (6)$$

To impose periodic boundary conditions (i.e., $\psi_0 = \psi_N$), as implied when using an angular coordinate such as φ, one sets $\mathbf{A}_{1N} = \mathbf{A}_{N1} = \mathbf{C}_{1N} = \mathbf{C}_{N1} = 1$. From the rotational energy barriers obtained from electronic structure calculations, it follows that the potential energy of the hindered methyl rotors can be parametrized by

$$V(\varphi) = c_0 + c_1 \sin(3\varphi) + c_2 \cos(3\varphi) + c_3 \sin(6\varphi)$$

$$+ c_4 \cos(6\varphi), \qquad (7)$$

with the parameters c_i obtained from least-squares linear regression. The resulting potential fits are shown in Supplemental Material, Fig. S4 (for adsorption of Ar atoms) and Fig. S5 (for adsorption of N_2 molecules) [41], and the corresponding parameters c_i are listed in Tables S1 and S4 [41], respectively. These tables illustrate that the inclusion of the $\cos(6\varphi)$ term plays an important role in obtaining an accurate fit. The barrier height is defined as the difference between the highest value of the rotational energy barrier (E_B) and the lowest rotational energy level (E_0), i.e., ($E_B - E_0$), to adequately take the zero-point energy of the rotor into account. The energy at which the experimental tunneling peak is located is compared with the energy of the rotational transition between the two lowest-energy levels ($0 \rightarrow 1$), i.e., ($E_1 - E_0$).

III. RESULTS AND DISCUSSION

The tunneling transitions appear in INS spectra recorded on the OSIRIS spectrometer [27–29] under high vacuum and at temperatures below 30 K as a well-defined peak at 0.33 meV [see the black spectra in Figs. 1(b) and 1(c)], matching the energy determined by Yildirim and co-workers [13] who studied the tunneling of methyl rotors in ZIF-8 without adsorbed guest molecules. When ZIF-8 is loaded with N_2 or Ar gas molecules, the tunneling peak changes its intensity and shifts in energy, signaling a change in the rotational energy of the rotors, which implies a change in their rotational barriers. These changes are induced by the interactions of the gas molecules with the framework. Individual tunneling spectra for increasing doses of the respective gases are shown in Figs. 1(b) and 1(c). These spectra were used to fit piecewise cubic Hermite interpolating polynomial lines through individual energy-transfer data points along the gas dose dimension. This allows us to construct 3D surfaces to reveal the evolution of the tunneling peak with increasing gas doses. The results are shown in Figs. 1(d) and 1(e), together with their 2D projections onto an energy-transfer (meV)−gas dose (molecules per unit cell) plane. Neutron powder-diffraction (NPD) patterns, collected together with the scattering spectra, are interpolated in the same way and plotted as 2D projections of 3D surfaces. INS spectra and NPD data are then plotted on a common gas dose axis with the corresponding BET adsorption isotherms for the same sample. Figures 2(a) and 2(b) show these results for N_2- and Ar-dosed ZIF-8, respectively.

Gas adsorption leads to changes in intensity and shifts of the tunneling peak for both N_2 and Ar dosing. The difference is that N_2 decreases the energy of the tunneling and eventually hinders it completely, whereas Ar increases the energy. Despite this opposite result, the level of gas loading at which these changes occur is within similar ranges that can be defined in terms of adsorption site occupancy. The levels for cumulative full occupancy of each adsorption site are shown as dashed-dotted lines in Figs. 2(a) and 2(b): at 8 molecules per unit cell (molec/uc) there is enough gas in the system to occupy all sites 1, by 32 molec/uc there is enough gas to occupy both sites 1 and sites 2, and so on (further details about adsorption sites are given in the Supplemental Material [41]). The phenomena observed in the adsorption isotherms, INS spectra, and NPD patterns all fit within these adsorption site brackets and should be understood to result from gas molecules occupying those adsorption sites. Figure 2(c) shows adsorption sites 1 to 5, previously identified by Moggach and co-workers [24]. *Ab initio* calculations were performed as part of this study to confirm this assertion of preferential adsorption sites playing a key role in observed tunneling phenomena. The results are summarized below.

Rotational energy barriers of a methyl top (rotor) upon Ar gas adsorption are shown in Fig. 2(d). The rotational barrier heights and the corresponding rotational transitions between the two lowest energy levels ($0 \rightarrow 1$) are listed in Table I for the "empty" ZIF-8 framework (i.e., without gas), and a sequential filling of the first three argon adsorption sites. The five lowest rotational energy levels are listed in Table S3 of the Supplemental Material [41]. For the empty framework, the experimental tunneling peak is observed at 0.33 meV [13],
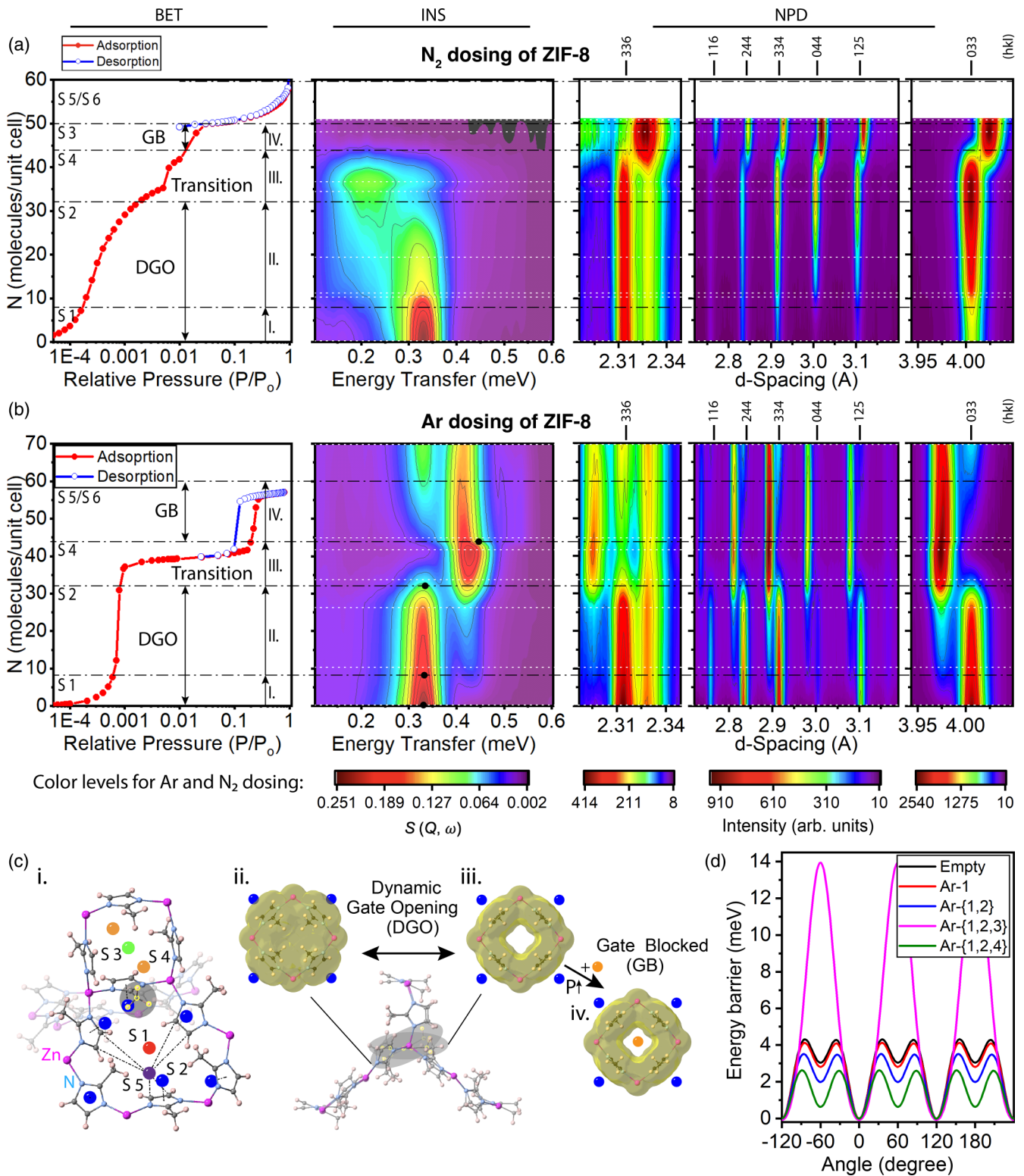
FIG. 2. (a), (b) BET adsorption measurements correlated with interpolated inelastic neutron-scattering spectra and interpolated neutron-diffraction patterns of ZIF-8 dosed with N_2 and Ar gas, respectively. BET measurements were performed at 77 K while neutron measurements were at 3 K. Dosing with gases for neutron experiments was done at 77 K to emulate BET adsorption conditions. Black dashed-dotted lines mark levels of cumulative full occupancy of each adsorption site. White dotted lines mark gas doses at which measurements were performed. (c)i Positions of adsorption sites 1 to 5 in ZIF-8, reproduced from Ref. [19]. Illustrations of average (c)ii closed and (c)iii open states (crystallographic information files (CIFs) from Ref. [14]) reached by 4-membered rings (4-MRs) as they undergo dynamic gate opening (DGO) motions. (c)iv 'Gate-blocked' (GB) state is illustrated as a result of site 4 occupied by gas molecules. van der Waals surfaces are marked in yellow. (d) Theoretically calculated rotational energy barrier of a methyl top in ZIF-8 with a sequential filling of the respective argon adsorption sites; for every adsorption site, all equivalent adsorption positions are occupied simultaneously.

TABLE I. Rotational constant B, optimal N–C–C–H dihedral angle φ_0, maximum of rotational barrier E_B, rotational energy barrier $E_B - E_0$, and energy $E_1 - E_0$ of $0 \rightarrow 1$ rotational transition for different Ar adsorption sites in ZIF-8. All energy quantities are given in meV. Theoretical energy $E_1 - E_0$ is scaled by a factor of 0.8 to resemble the experimental tunneling peak of empty ZIF-8 at 0.33 meV. Note that scaled theoretical values applied here are for ease of comparison with experimental data and do not alter any conclusions.

	No. Ar atoms	B	φ_0 (°)	E_B	$E_B - E_0$	$E_1 - E_0$	$(E_1 - E_0)*0.8$
ZIF-8 (empty)	0	0.573	88.2	4.308	1.821	0.410	0.328
ZIF-8 + Ar-1	8	0.573	88.2	4.119	1.728	0.428	0.342
ZIF-8 + Ar-{1, 2}	32	0.573	88.2	3.511	1.475	0.487	0.389
ZIF-8 + Ar-{1, 2, 3}	38	0.574	86.9	13.95	10.97	0.071	0.057
ZIF-8 + Ar-{1, 2, 4}	44	0.573	88.1	2.623	1.214	0.560	0.448

which is slightly overestimated computationally, yielding a value of 0.41 meV. In contrast, it is worth noting that Ruggiero and co-workers [42] reported a substantially lower computational value of 0.225 meV for the first rotational transition, which is in discrepancy with experiments.

When filling the first type of adsorption sites in ZIF-8 (denoted as Ar-1), requiring a total of 8 argon atoms per unit cell, the energy of the first rotational transition ($E_1 - E_0$) remains virtually unaltered (Table I). If also the second type of adsorption sites (denoted as Ar-2) are filled, yielding a total of 32 argon atoms across sites 1 and 2 per unit cell, the rotational energy barrier (E_B) of the methyl top is lowered by about 0.6 meV, resulting in a modest increase in the energy of the first rotational transition. The addition of 6 further argon atoms per unit cell, occupying the third type of adsorption sites (denoted as Ar-3, as highlighted in Table I), substantially increases the rotational energy barrier so that the energy of the first rotational transition decreases drastically to 0.07 meV, and the methyl top changes its behavior from a quasifree rotor to an almost hindered rotor, frozen in a particular rotation state. However, suppose the fourth type of adsorption site (denoted as Ar-4) is occupied instead of the third type (Ar-3). In that case, the rotational energy barrier of the methyl top decreases instead of increasing so that the energy of the first rotational transition rises, similar to the experimentally observed trend. This finding concludes that site 3 is not filled during subatmospheric adsorption experiments (unlike at high pressure [24]); otherwise, the tunneling peak would have disappeared at a dose of 38 molec/uc, which contradicts our experimental observations.

Likewise, *ab initio* calculations were performed to interrogate the effects of N_2 adsorption on the rotational tunneling energy of ZIF-8 (see details in Sec. II). As in the case of Ar, the computational results (Table S5 [41]) predict that after filling the first and second adsorption sites, the additional nitrogen molecules occupy the fourth type of adsorption sites, rather than the third type. For this adsorption sequence, the first rotational transition ($E_1 - E_0$) decreases by about $0.02 - 0.04$ meV after the initial adsorption of N_2 (by the occupation of sites 1 and 2). When also filling adsorption sites 4, the rotational transition decreased further by 0.07 meV, so that the tunneling transition is lowered by ~ 0.1 meV with respect to the empty ZIF-8, hence in good agreement with the experimental INS spectra [Fig. 2(a)] where the tunneling peak is shifted to lower energy. Subsequently, it is observed experimentally that the tunneling peaks disappear [Fig. 1(b)], which suggests the nitrogen molecules eventually do start to

occupy site 3, for which *ab initio* calculations (Table S5 [41]) predicted a high rotational energy barrier (E_B).

Based on the tunneling phenomena, the adsorption process of ZIF-8 can be subdivided into four stages, as designated in Figs. 2(a) and 2(b). The first stage (I)—between 0 and 8 molec/uc—supplies enough gas to occupy all sites 1 [designated as S1 in Fig. 2(c)]. This phase is the initial loading of the framework, during which the isotherm starts sloping upwards while the intensity of the tunneling peak decreases. Therefore, no shifts of INS or NPD peaks occur during this phase.

The second stage (II)–between 8 and 32 molec/uc—supplies enough gas to occupy all sites 2 in addition to sites 1. During this phase the isotherm rises rapidly for both gases, but more so for Ar. The tunneling peak at around 0.33 meV decreases gradually, and the "dosed" tunneling peaks emerge at energies of 0.22 meV for N_2 and 0.42 meV for Ar. This change in energy of the tunneling peak is not gradual, however. The tunneling energy shifts from one energy to another for some methyl rotors before others, but the shift is sudden rather than gradual. This shift is not completed until the end of the next stage of the adsorption process.

The third stage (III)–between 32 and 44 molec/uc—fills sites 4 in addition to sites 1 and 2. Isotherms level off in this phase before turning upwards again, the tunneling peaks convert completely to their lower and higher energies for N_2 and Ar, respectively, and shifts in NPD peaks occur for both gases: for N_2, the unit cell of ZIF-8 expands (1.4% volumetric expansion), while for Ar, it contracts (2.2% volumetric contraction). These contrasting changes for the two gases show that despite being considered inert at these conditions, adsorption of these gases results in physicochemical interactions with the framework, which produce changes in local potentials and accumulate to trigger structural transformation in the long-range order of the framework. Furthermore, we propose that these contrasting changes are, for instance, influenced by the difference in size of the guest molecules (N_2 > Ar) or the quadrupole moment of N_2, rendering differential host-guest interactions, albeit unraveling the precise mechanism responsible for this effect will warrant further investigation.

In the fourth stage (IV)—for Ar, between 44 and 60 molec/uc—sites 5 and 6 are filled in addition to sites 1, 2, and 4. Hysteresis loops can be seen forming in the adsorption-desorption isotherms [16]. Our results suggest that the interaction energies at specific adsorption sites have a role to play in the observed effect. More precisely, the tunneling peak does not disappear for Ar, but it splits into

three components—indicating that different methyl groups see three types of environments. Crucially, however, the 0.42-meV tunneling peak dominates the additional higher- and lower-energy peaks. Therefore, the methyl groups of ZIF-8 subject to high Ar loading still exhibit rotational tunneling, albeit at different energies. For N_2 adsorption, however, the tunneling peaks observed in experiments completely disappear after site 3 starts to be occupied [Fig. 2(a)]. A full occupation of site 3 occurs at 50 molec/uc, coinciding with the point at which the experimental adsorption isotherm also changes in shape.

IV. CONCLUDING REMARKS

Our experimental results supplemented with *ab initio* calculations show that the reported adsorption sites hierarchy based on interaction energy inside the ZIF-8 pores (observed under GPa pressure by Moggach and co-workers [24]) holds for low-pressure conditions with one exception: the adsorption sites inside 4-membered rings [sites 3 in Fig. 2(c)] of ZIF-8 are not occupied by argon gas molecules at subatmospheric pressure. Nevertheless, for both gases the adsorption sites on either side of the four-membered rings (4-MRs, sites 4) are indeed occupied when enough gas is supplied, which is key to understanding ZIF-8′s adsorption behavior: the steps in adsorption isotherms and the shifts in long-range order of ZIF-8 occur after sites 1 and 2 have been filled and in the process of filling sites 4 [see Figs. 2(a) and 2(b)]. Structurally, this necessitates linker rotations to make sites 4 accessible— the dynamic "gate-opening" motions—explaining the results observed in other experiments [see Figs. 2(c)ii and 2(c)iii for a schematic]. However, it also implies a "gate-blocked" structure in which the linkers of ZIF-8 are no longer able to rotate to a gate-closed position due to guest molecules adsorbed in sites 4 [see Figs. 2(c)iii and 2(c)iv for a schematic]—this is accompanied by a shift in the long-range order of the framework observed in neutron powder-diffraction patterns [Figs. 2(a) and 2(b)].

In conclusion, *in situ* high-resolution INS spectroscopy [27–29] observes the methyl tunneling rotors while simultaneously yielding neutron powder-diffraction patterns containing structural information. This combination enriches gas adsorption isotherms with previously unobserved insights, and could inspire future investigations of porous hybrid materials exhibiting tunneling phenomena.

[1] D. Fairen-Jimenez, S. A. Moggach, M. T. Wharmby, P. A. Wright, S. Parsons, and T. Düren, J. Am. Chem. Soc. **133**, 8900 (2011).

[2] W. Morris, C. J. Stevens, R. E. Taylor, C. Dybowski, O. M. Yaghi, and M. A. Garcia-Garibay, J. Phys. Chem. C **116**, 13307 (2012).

[3] *Mechanical Behaviour of Metal–Organic Framework Materials*, edited by J. C. Tan (The Royal Society of Chemistry, London, UK, 2023).

[4] A. Comotti, S. Bracco, and P. Sozzani, Acc. Chem. Res. **49**, 1701 (2016).

[5] M. R. Ryder, B. Van de Voorde, B. Civalleri, T. D. Bennett, S. Mukhopadhyay, G. Cinque, F. Fernandez-Alonso, D. De Vos, S. Rudic, and J. C. Tan, Phys. Rev. Lett. **118**, 255502 (2017).

[6] A. Gonzalez-Nelson, F. X. Coudert, and M. A. van der Veen, Nanomaterials **9**, 330 (2019).

[7] M. R. Ryder, B. Civalleri, T. D. Bennett, S. Henke, S. Rudić, G. Cinque, F. Fernandez-Alonso, and J. C. Tan, Phys. Rev. Lett. **113**, 215502 (2014).

[8] F. Formalik, B. Mazur, M. Fischer, L. Firlej, and B. Kuchta, J. Phys. Chem. C **125**, 7999 (2021).

[9] R. Freund, S. Canossa, S. M. Cohen, W. Yan, H. Deng, V. Guillerm, M. Eddaoudi, D. G. Madden, D. Fairen-Jimenez, H. Lyu *et al.*, Angew. Chem. Int. Ed. **60**, 23946 (2021).

[10] *Neutron Scattering − Fundamentals*, edited by F. Fernandez-Alonso and D. L. Price (Academic Press, New York, 2013).

[11] J. Eckert, Spectroc. Acta A: Mol. Biomol. Spectrosc. **48**, 271 (1992).

[12] M. Prager and A. Heidemann, Chem. Rev. **97**, 2933 (1997).

[13] W. Zhou, H. Wu, T. J. Udovic, J. J. Rush, and T. Yildirim, J. Phys. Chem. A **112**, 12602 (2008).

[14] S. A. Moggach, T. D. Bennett, and A. K. Cheetham, Angew. Chem. Int. Ed. **48**, 7087 (2009).

[15] D. Fairen-Jimenez, R. Galvelis, A. Torrisi, A. D. Gellan, M. T. Wharmby, P. A. Wright, C. Mellot-Draznieks, and T. Duren, Dalton Trans. **41**, 10752 (2012).

[16] C. O. Ania, E. Garcia-Perez, M. Haro, J. J. Gutierrez-Sevillano, T. Valdes-Solis, J. B. Parra, and S. Calero, J. Phys. Chem. Lett. **3**, 1159 (2012).

[17] N. Y. Tan, M. T. Ruggiero, C. Orellana-Tavra, T. Tian, A. D. Bond, T. M. Korter, D. Fairen-Jimenez, and J. A. Zeitler, Chem. Commun. **51**, 16037 (2015).

[18] T. Tanno, Y. Watanabe, K. Umeno, A. Matsuoka, H. Matsumura, M. Odaka, and N. Ogawa, J. Phys. Chem. C **121**, 17921 (2017).

[19] D. I. Kolokolov, A. G. Stepanov, and H. Jobic, J. Phys. Chem. C **119**, 27512 (2015).

[20] F. Formalik, M. Fischer, J. Rogacka, L. Firlej, and B. Kuchta, Micropor. Mesopor. Mat **304**, 109132 (2020).

[21] F. X. Coudert, ChemPhysChem **18**, 2732 (2017).

[22] G. Chaplais, G. Fraux, J.-L. Paillaud, C. Marichal, H. Nouali, A. H. Fuchs, F.-X. Coudert, and J. Patarin, J. Phys. Chem. C **122**, 26945 (2018).

[23] C. L. Hobday, T. D. Bennett, D. Fairen-Jimenez, A. J. Graham, C. A. Morrison, D. R. Allan, T. Duren, and S. A. Moggach, J. Am. Chem. Soc. **140**, 382 (2018).

[24] C. L. Hobday, C. H. Woodall, M. J. Lennox, M. Frost, K. Kamenev, T. Duren, C. A. Morrison, and S. A. Moggach, Nat. Commun. **9**, 1429 (2018).

[25] *Neutron Scattering–Magnetic and Quantum Phenomena*, edited by F. Fernandez-Alonso and D. L. Price (Academic Press, New York, 2015).

[26] *Neutron Scattering–Applications* in *Biology, Chemistry, and Materials Science*, edited by F. Fernandez-Alonso and D. L. Price (Academic Press, New York, 2017).

[27] F. Demmel, D. McPhail, J. Crawford, D. Maxwell, K. Pokhilchuk, V. Garcia-Sakai, S. Mukhopadyay, M. T. F. Telling, F. J. Bermejo, N. T. Skipper *et al.*, EPJ Web. Conf. **83**, 03003 (2015).

[28] M. T. F. Telling and K. H. Andersen, Phys. Chem. Chem. Phys. **7**, 1255 (2005).

[29] M. T. F. Telling, S. I. Campbell, D. Engberg, Y. M. D. Martin, and K. H. Andersen, Phys. Chem. Chem. Phys. **18**, 8243 (2016).

[30] T. L. Easun, F. Moreau, Y. Yan, S. H. Yang, and M. Schroder, Chem. Soc. Rev. **46**, 239 (2017).

[31] J. VandeVondele, M. Krack, F. Mohamed, M. Parrinello, T. Chassaing, and J. Hutter, Comput. Phys. Commun. **167**, 103 (2005).

[32] J. Hutter, M. Iannuzzi, F. Schiffmann, and J. VandeVondele, WIREs Comput. Mol. Sci. **4**, 15 (2014).

[33] A. Hjorth Larsen, J. Jorgen Mortensen, J. Blomqvist, I. E. Castelli, R. Christensen, M. Dulak, J. Friis, M. N. Groves, B. Hammer, C. Hargus *et al.*, J. Phys.: Condens. Matter. **29**, 273002 (2017).

[34] J. P. Perdew, K. Burke, and M. Ernzerhof, Phys. Rev. Lett. **77**, 3865 (1996).

[35] S. Grimme, J. Antony, S. Ehrlich, and H. Krieg, J. Chem. Phys. **132**, 154104 (2010).

[36] S. Grimme, S. Ehrlich, and L. Goerigk, J. Comput. Chem. **32**, 1456 (2011).

[37] S. Goedecker, M. Teter, and J. Hutter, Phys. Rev. B **54**, 1703 (1996).

[38] J. VandeVondele and J. Hutter, J. Chem. Phys. **127**, 114105 (2007).

[39] J. Izaac and J. Wang, *Computational Quantum Mechanics* (Springer, Cham, Switzerland, 2018).

[40] M. Pillai, J. Goglio, and T. G. Walker, Am. J. Phys. **80**, 1017 (2012).

[41] See Supplemental Material at http://link.aps.org/supplemental/10.1103/PhysRevMaterials.7.073402 for supplemental text on ZIF-8 adsorption sites; supplemental figures on different adsorption sites in sodalite cage of ZIF-8; crystallographic adsorption sites; temperature ramp study of the methyl tunneling of empty ZIF-8 under high vacuum; calculated rotational energy barrier of a methyl top in ZIF-8 with filling of Ar or N_2; and supplemental tables of the calculated rotational energies of the methyl rotor in empty ZIF-8 and with sequential filling of Ar or N_2. The Supplemental Material also contains Ref. [23].

[42] Q. Li, A. J. Zaczek, T. M. Korter, J. A. Zeitler, and M. T. Ruggiero, Chem. Commun. **54**, 5776 (2018).